Supervised Descent Learning for Thoracic Electrical Impedance Tomography

Ke Zhang, Rui Guo, *Student Member, IEEE*, Maokun Li, *Senior Member, IEEE*, Fan Yang, *Fellow, IEEE*, Shenheng Xu, *Member, IEEE*, and Aria Abubakar, *Senior Member, IEEE*

Abstract—Objective: The absolute image reconstruction problem of electrical impedance tomography (EIT) is ill-posed. Traditional methods usually solve a nonlinear least squares problem with some kind of regularization. These methods suffer from low accuracy, poor anti-noise performance, and long computation time. Besides, the integration of *a priori information* is not very flexible. This work tries to solve EIT inverse problem using a machine learning algorithm for the application of thorax imaging. *Methods:* We developed the supervised descent learning EIT (SDL-EIT) inversion algorithm based on the idea of supervised descent method (SDM). The algorithm approximates the mapping from measured data to the conductivity image by a series of descent directions learned from training samples. We designed a training data set in which the thorax contour and some general structure of lungs and heart are embedded. The algorithm is implemented in both two- and three-dimensional cases, and is evaluated using synthetic and measured thoracic data. *Results and conclusion:* For synthetic data, SDL-EIT shows better accuracy and anti-noise performance compared with traditional Gauss–Newton inversion (GNI) method. For measured data, the result of SDL-EIT is reasonable compared with computed tomography (CT) scan image. *Significance:* Using SDL-EIT, prior information can be easily integrated through the specifically designed training data set, and the image reconstruction process can be accelerated. The algorithm is effective in inverting measured thoracic data. It is a potential algorithm for human thorax imaging.

*Index Terms—*Electrical impedance tomography, inverse problem, machine learning, supervised descent method, thorax imaging.

I. INTRODUCTION

ELECTRICAL impedance tomography (EIT) is a medical imaging modality that can reconstruct the conductivity distribution interior of a medical target [1]–[5]. In the measurement of EIT, a number of electrodes are fixed around the medical target. Then small alternating currents are injected and the induced voltages are measured at the surface through the electrodes according to a certain protocol.

EIT is most often applied in thorax imaging. In the human thorax, the conductivities of main organs or tissues, such as

the muscle, lung, and heart, have large differences. On the other hand, many lung diseases, such as the pneumothorax, pleural effusion, and pulmonary edema, show an abnormity of air or liquid content and distribution in the thorax, which may significantly influence the conductivity distribution. Since EIT is sensitive to the air or liquid changes, it is a promising tool for bedside monitoring of their contents and distributions.

The absolute EIT image reconstruction faces several challenges. Firstly, the accuracy of reconstruction is very sensitive to modeling errors and measurement noise. This is due to the ill-posedness of EIT image reconstruction problem. Secondly, the image reconstruction process is computationally intensive. As a result, it is hard to fulfill the requirement of real-time monitoring. One promising solution is the development of direct reconstruction methods such as the D-bar method [6]–[9], the factorization method [10], [11], [12], and the block method [13]. The references here are far from complete due to the page limit and the authors' limited knowledge.

On the other hand, machine learning techniques are promising to deal with the above challenges. Firstly, *a priori information* can be integrated in a flexible manner through training data. It can help to enhance the accuracy of reconstruction. Secondly, the image reconstruction can be fast once a machine learning model has been trained.

Recently, machine learning techniques, especially deep learning, have been successfully applied to EIT image reconstruction. These methods can be roughly classified into two categories: (1) methods mapping from image to image and (2) methods mapping from data to image. For the first type of methods, a relatively low-resolution image is obtained from some traditional methods, then it is used as the input of a machine learning model, and finally an image with enhanced resolution is output. These methods have been successfully applied for EIT difference reconstruction [14], [15] and EIT absolute reconstruction [16], [17]. For the second type of methods, the mapping from measured data to image is directly estimated by machine learning models. Such methods have been applied for EIT difference reconstruction [18], [19], [20] and EIT absolute reconstruction [21], [22], [23]. Typically, in [20], EIT images are represented on a low dimensional manifold, and the mapping from data to encoded image is estimated. This converts the EIT inverse problem from an ill-posed one to an approximately well-posed one. In [23], the mapping from data to image is estimated in an unsupervised manner. For a review on EIT using machine learning algorithms, please refer to [24].

In this work, we developed a supervised descent learning

EIT inversion algorithm, called SDL-EIT, based on the idea of supervised descent method (SDM). SDM is first proposed by Xiong and De la Torre [25] in the field of computer vision. It is a powerful machine learning algorithm for solving nonlinear least squares problems. Recently, the idea of SDM has been successfully applied to microwave imaging [26] and geophysical electromagnetic data inversion [27], and the results show impressive generalization ability. In this paper, we applied the framework of SDM to nonlinear EIT inverse problem, focusing on the application of absolute thoracic imaging. Prior information about general thoracic structures can be easily integrated through specifically designed training samples. By inverting synthetic data, SDL-EIT shows better anti-noise performance than the Gauss–Newton inversion method (see the quantified results in Section IV-B and V-B), and shows reasonable prediction results on test models unseen in the training. SDL-EIT is also tested using measured thoracic data, and the results show a correlation with the CT scan image.

This paper is organized as follows. In Section II, EIT forward problem is introduced. In Section III, the SDL-EIT algorithm is formulated. Section IV–VI present the inversion results using two-dimensional (2D) synthetic data, three-dimensional (3D) synthetic data, and measured thoracic data, respectively. Discussion is made in Section VII. Conclusion is drawn in Section VIII.

II. EIT FORWARD PROBLEM

EIT forward problem refers to the calculation of electric potential $\phi(\mathbf{r})$ ($\mathbf{r}$ is the spatial position) in the imaging domain $\Omega \subset \mathbb{R}^n (n = 2, 3)$ given injected currents and conductivity distribution $\sigma(\mathbf{r})$. In this work, we adopt the widely used complete electrode model (CEM) [28], which consists of the following equations:

$$
\begin{cases}
\nabla \cdot (\sigma(\mathbf{r})\nabla\phi(\mathbf{r})) = 0 & \mathbf{r} \in \Omega, \\
\int_{\partial\Omega_\ell} \sigma(\mathbf{r})\nabla\phi(\mathbf{r}) \cdot \hat{n} ds = I_\ell & \ell = 1, 2, \ldots, L, \\
\sigma(\mathbf{r})\nabla\phi(\mathbf{r}) \cdot \hat{n} = 0 & \mathbf{r} \in \partial\Omega/(\partial\Omega_1 \cup \ldots \cup \partial\Omega_L), \\
\phi(\mathbf{r}) + z_\ell\sigma(\mathbf{r})\nabla\phi(\mathbf{r}) \cdot \hat{n} = V_\ell & \mathbf{r} \in \partial\Omega_\ell, \; \ell = 1, 2, \ldots, L, \\
\sum_{\ell=1}^{L} I_\ell = 0, \quad \sum_{\ell=1}^{L} V_\ell = 0,
\end{cases}
\tag{1}
$$

where $\partial\Omega$ is the boundary of Ω, $\partial\Omega_\ell$ is the boundary covered by Electrode ℓ, $\hat{n}$ is the outward unit normal vector to $\partial\Omega$, I_ℓ is the injected current to Electrode ℓ, L is the total number of electrodes, z_ℓ is the contact impedance of Electrode ℓ, and V_ℓ is the electric potential on Electrode ℓ.

The above boundary-value problem can be solved numerically. In this work, we used the finite element method (FEM) [29], [30]. For the injection-measurement scheme, we used the adjacent protocol, in which currents are injected through adjacent electrodes, and the induced voltages are measured on non-current-carrying adjacent electrodes.

III. SUPERVISED DESCENT LEARNING EIT INVERSION ALGORITHM

In the following derivation, we use bold characters to represent column vectors or matrices. The forward model that is used to generate boundary voltages is denoted as $\mathbf{s}(\boldsymbol{\sigma})$ where $\boldsymbol{\sigma}$ is a discrete representation of the conductivity. The measured data is denoted as $\mathbf{d}_*$. EIT inversion can be formulated as minimizing the following objective function:

$$
C(\boldsymbol{\sigma}) = ||\mathbf{s}(\boldsymbol{\sigma}) - \mathbf{d}_*||^2,
\tag{2}
$$

where $|| \cdot ||$ denotes the $L2$ norm. This is a nonlinear least squares problem because $\mathbf{s}(\boldsymbol{\sigma})$ is nonlinear w.r.t. $\boldsymbol{\sigma}$.

In the Gauss–Newton method, an initial guess $\boldsymbol{\sigma}_0$ is set before the iteration process. In this case, the problem (2) is equivalent to finding $\Delta\boldsymbol{\sigma} = \boldsymbol{\sigma} - \boldsymbol{\sigma}_0$ that minimizes:

$$
C(\boldsymbol{\sigma}_0 + \Delta\boldsymbol{\sigma}) = ||\mathbf{s}(\boldsymbol{\sigma}_0 + \Delta\boldsymbol{\sigma}) - \mathbf{d}_*||^2.
\tag{3}
$$

Assume the forward model $\mathbf{s}(\boldsymbol{\sigma})$ is twice differentiable, and then (3) can be approximated by a second order Taylor expansion:

$$
C(\boldsymbol{\sigma}_0 + \Delta\boldsymbol{\sigma}) \approx C(\boldsymbol{\sigma}_0) + \mathbf{J}_C(\boldsymbol{\sigma}_0)^T \cdot \Delta\boldsymbol{\sigma} + \frac{1}{2}\Delta\boldsymbol{\sigma}^T \cdot \mathbf{H}(\boldsymbol{\sigma}_0) \cdot \Delta\boldsymbol{\sigma},
\tag{4}
$$

where $\mathbf{J}_C(\boldsymbol{\sigma}_0)$ and $\mathbf{H}(\boldsymbol{\sigma}_0)$ are the Jacobian and Hessian of C at $\boldsymbol{\sigma}_0$, respectively. The minimum of (4) can be obtained by taking the derivative of $C(\boldsymbol{\sigma}_0 + \Delta\boldsymbol{\sigma})$ w.r.t. $\Delta\boldsymbol{\sigma}$ and letting the result equal zero. The minimum is shown as follows:

$$
\Delta\boldsymbol{\sigma}_1 = -\mathbf{H}(\boldsymbol{\sigma}_0)^{-1} \cdot \mathbf{J}_C(\boldsymbol{\sigma}_0).
\tag{5}
$$

After some derivation, it is easy to show that $\mathbf{J}_C(\boldsymbol{\sigma}_0) = 2\mathbf{J}_\mathbf{s}(\boldsymbol{\sigma}_0)^T \cdot (\mathbf{s}(\boldsymbol{\sigma}_0) - \mathbf{d}_*)$, where $\mathbf{J}_\mathbf{s}$ is the Jacobian of the forward model. Then (5) becomes:

$$
\Delta\boldsymbol{\sigma}_1 = -2\mathbf{H}(\boldsymbol{\sigma}_0)^{-1}\mathbf{J}_\mathbf{s}(\boldsymbol{\sigma}_0)^T \cdot (\mathbf{s}(\boldsymbol{\sigma}_0) - \mathbf{d}_*).
\tag{6}
$$

Equation (6) can be further written as:

$$
\Delta\boldsymbol{\sigma}_1 = \mathbf{K}_1 \cdot \Delta\mathbf{d}_1,
\tag{7}
$$

where $\mathbf{K}_1 = -2\mathbf{H}(\boldsymbol{\sigma}_0)^{-1}\mathbf{J}_\mathbf{s}(\boldsymbol{\sigma}_0)^T$ and $\Delta\mathbf{d}_1 = \mathbf{s}(\boldsymbol{\sigma}_0) - \mathbf{d}_*$. Equation (7) is the first update of the Gauss–Newton method. The matrix $\mathbf{K}_1$ is related to the Jacobian and Hessian, the numerical approximation of which is usually computationally expensive. The vector $\Delta\mathbf{d}_1$ is the difference between the simulated data using the initial guess and the measured data. The matrix $\mathbf{K}_1$ can be viewed as a mapping from the data space to the model space.

Based on the idea of supervised descent method (SDM) [25], the matrix $\mathbf{K}_1$ can be learned from training data by linear regression. Specifically, given training samples of $\Delta\boldsymbol{\sigma}_1$ and $\Delta\mathbf{d}_1$, we can estimate $\mathbf{K}_1$ by performing a linear regression between them. The details are as follows.

A. SDL-EIT Training

Assume we have a set of training models $\{\boldsymbol{\sigma}_*^i\}$ and their corresponding data $\{\mathbf{d}_*^i\}$. Then we choose the initial guess for these training models as $\{\boldsymbol{\sigma}_0^i\}$. We used same initial guesses for different training models in our experiments. By running the forward simulation, we can obtain simulated data $\{\mathbf{s}(\boldsymbol{\sigma}_0^i)\}$ corresponding to the initial guesses. Then the learning process is to solve the following linear regression problem:

$$\arg\min_{\mathbf{K}_1} \sum_i ||\Delta\boldsymbol{\sigma}_1^{*i} - \mathbf{K}_1 \cdot \Delta\mathbf{d}_1^i||^2, \qquad (8)$$

where $\Delta\boldsymbol{\sigma}_1^{*i} = \boldsymbol{\sigma}_*^i - \boldsymbol{\sigma}_0^i$ and $\Delta\mathbf{d}_1^i = \mathbf{s}(\boldsymbol{\sigma}_0^i) - \mathbf{d}_*^i$. It is worth noting that $\Delta\boldsymbol{\sigma}_1^{*i}$ has a slightly different meaning from $\Delta\boldsymbol{\sigma}_1$ in (7). The $\Delta\boldsymbol{\sigma}_1^{*i}$ is the difference between the correct model and the initial guess, while $\Delta\boldsymbol{\sigma}_1$ is the difference between the model after the first iteration and the initial guess. This may enable the algorithm to learn a global descent direction to some extent.

The EIT forward model $\mathbf{s}(\boldsymbol{\sigma})$ is nonlinear. As a result, it is unlikely for the algorithm to reach the true solution using only one step of learning. Therefore, the above learning process is iterated. In the kth iteration, the models $\{\boldsymbol{\sigma}_{k-1}^i\}$ are known. Then the linear regression problem becomes:

$$\arg\min_{\mathbf{K}_k} \sum_i ||\Delta\boldsymbol{\sigma}_k^{*i} - \mathbf{K}_k \cdot \Delta\mathbf{d}_k^i||^2, \qquad (9)$$

where $\Delta\boldsymbol{\sigma}_k^{*i} = \boldsymbol{\sigma}_*^i - \boldsymbol{\sigma}_{k-1}^i$, $\Delta\mathbf{d}_k^i = \mathbf{s}(\boldsymbol{\sigma}_{k-1}^i) - \mathbf{d}_*^i$, and $\mathbf{K}_k$ is the descent direction in the kth iteration. The above problem can be solved by using least squares solver. After solving for $\mathbf{K}_k$, the model can be updated as:

$$\boldsymbol{\sigma}_k^i = \boldsymbol{\sigma}_{k-1}^i + \mathbf{K}_k \cdot \Delta\mathbf{d}_k^i. \qquad (10)$$

The iteration can be terminated when the model or data loss becomes sufficiently low. Here we define a model loss as:

$$Loss_M = \frac{1}{N} \sum_{i=1}^{N} \frac{||\boldsymbol{\sigma}_k^i - \boldsymbol{\sigma}_*^i||}{||\boldsymbol{\sigma}_*^i||}, \qquad (11)$$

where N is the total number of training samples. Similarly, a data loss can be defined as:

$$Loss_D = \frac{1}{N} \sum_{i=1}^{N} \frac{||\mathbf{s}(\boldsymbol{\sigma}_k^i) - \mathbf{d}_*^i||}{||\mathbf{d}_*^i||}. \qquad (12)$$

After the training process, we can obtain a set of descent directions $\{\mathbf{K}_k\}$ which are ready for the inversion of new measured data. It is worth mentioning that a linear EIT reconstruction matrix is obtained in [31] from the regression of training data, and the idea used is very similar to the first update of the above training process.

B. SDL-EIT Inference

In the inference stage, new data can be inverted using the learned descent directions. The details are as follows. Given measured data $\mathbf{d}_{obs}$ and an initial guess $\boldsymbol{\sigma}_0$, the model can be updated iteratively as:

$$\boldsymbol{\sigma}_k = \boldsymbol{\sigma}_{k-1} + \mathbf{K}_k \cdot (\mathbf{s}(\boldsymbol{\sigma}_{k-1}) - \mathbf{d}_{obs}). \qquad (13)$$

The initial guess $\boldsymbol{\sigma}_0$ is chosen the same as those used in the training process. Similar to (12), we can also define a loss to measure the data misfit. The inversion process can be stopped when the loss is smaller than a prescribed value.

C. Implementation Details

The learning of SDL-EIT is accomplished by solving the linear regression problem (9). In the implementation, the model differences $\{\Delta\boldsymbol{\sigma}_k^{*i}\}$ at the kth step are arranged into a matrix $\Delta\boldsymbol{\Sigma}_k$. The ith row of $\Delta\boldsymbol{\Sigma}_k$ represents one sample $(\Delta\boldsymbol{\sigma}_k^{*i})^T$. Similarly, the data differences $\{\Delta\mathbf{d}_k^i\}$ are also arranged into a matrix $\Delta\mathbf{D}_k$, the ith row of which represents one sample $(\Delta\mathbf{d}_k^i)^T$. Then solving (9) is equivalent to solving

$$\arg\min_{\mathbf{K}_k} ||\Delta\boldsymbol{\Sigma}_k - \Delta\mathbf{D}_k \cdot \mathbf{K}_k^T||^2. \qquad (14)$$

The solution of the above problem can be written into a closed form:

$$\mathbf{K}_k^T = (\Delta\mathbf{D}_k^T \cdot \Delta\mathbf{D}_k)^{-1} \cdot \Delta\mathbf{D}_k^T \cdot \Delta\boldsymbol{\Sigma}_k. \qquad (15)$$

This solution may be unstable when $\Delta\mathbf{D}_k^T \cdot \Delta\mathbf{D}_k$ is close to singular. In order to stabilize the solution, we use the singular value decomposition (SVD) and a damping factor. Assume the SVD of $\Delta\mathbf{D}_k$ is $\Delta\mathbf{D}_k = \mathbf{U} \cdot \boldsymbol{\Lambda} \cdot \mathbf{V}^T$, where $\mathbf{U}$ and $\mathbf{V}$ are unitary matrices, and $\boldsymbol{\Lambda}$ is a diagonal matrix. Substitute the SVD of $\Delta\mathbf{D}_k$ into (15) and apply the damping factor, we have

$$\mathbf{K}_k^T = \mathbf{V} \cdot (\boldsymbol{\Lambda}^T \cdot \boldsymbol{\Lambda} + \alpha\mathbf{I})^{-1} \cdot \boldsymbol{\Lambda}^T \cdot \mathbf{U}^T \cdot \Delta\boldsymbol{\Sigma}_k, \qquad (16)$$

where $\mathbf{I}$ is the identity matrix, and α is the damping factor. In our experiments, the value of α is set to have the same order of magnitude as the maximum singular value of $\Delta\mathbf{D}_k$.

IV. 2D SIMULATION EXPERIMENT

A. Training

All the training samples are defined on a finite-element thorax model with 2086 nodes and 4040 triangles. The boundary of the model was extracted from a slice of CT scan image. Sixteen electrodes are approximately evenly distributed on the boundary, covering 73% of the whole boundary.

The training data set was designed to contain two types of samples, as illustrated in Fig. 1. The 1-circle samples contain only one circle (C) with random location and conductivity. The radius of the circle r is fixed as 0.03 m. Based on our experience, the radius of the circle can be set as other proper values. The conductivity of the circle is uniform randomly sampled in [0.06, 0.36] S/m, and the conductivity of the background is uniform randomly sampled in [0.2, 0.25] S/m.

The design of the 3-ellipse samples is inspired by Wei *et al* [17]. Each sample contains three ellipses (e1, e2, and e3) with random locations, sizes, rotation angles, and conductivities. The parameter ranges of the ellipses are listed in Table I. In all the samples, the conductivity of the background is uniform randomly sampled in [0.2, 0.25] S/m.
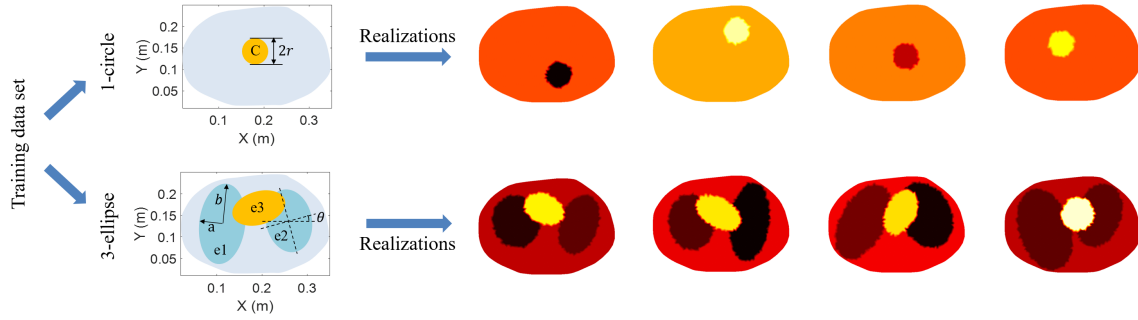
Fig. 1. Design of 2D training data set. The whole data set contains two types of samples: 1-circle samples and 3-ellipse samples. The 1-circle samples contain only one circle (C) with random location and conductivity. The radius of the circle is denoted as r. The 3-ellipse samples contain three ellipses (e1, e2, and e3) with random locations, sizes, rotation angles, and conductivities. The x-radius and y-radius of the ellipse is denoted as a and b, respectively. The rotation angle of the ellipse is denoted as θ. Some random realizations of the two types of samples are also shown.

TABLE I
SETTINGS OF THE 3-ELLIPSE TRAINING SAMPLES (ALL THE PARAMETERS ARE UNIFORM RANDOMLY SAMPLED FROM THE CORRESPONDING SETS.)

Ellipse / Parameter	e1	e2	e3
Center location	$\{(x,y)\|x \in [0.103, 0.129]\,\text{m}, y \in [0.117, 0.15]\,\text{m}\}$	$\{(x,y)\|x \in [0.238, 0.262]\,\text{m}, y \in [0.124, 0.159]\,\text{m}\}$	$\{(x,y)\|x \in [0.178, 0.197]\,\text{m}, y \in [0.155, 0.172]\,\text{m}\}$
Size	x-radius $\in [0.04, 0.07]\,\text{m}$, y-radius $\in [0.06, 0.12]\,\text{m}$	x-radius $\in [0.04, 0.07]\,\text{m}$, y-radius $\in [0.06, 0.12]\,\text{m}$	x-radius $\in [0.02, 0.06]\,\text{m}$, y-radius $\in [0.02, 0.06]\,\text{m}$
Rotation angle	$[-\pi/6, \pi/6]\,\text{rad}$	$[-\pi/6, \pi/6]\,\text{rad}$	$[-\pi/6, \pi/6]\,\text{rad}$
Conductivity	$[0.06, 0.16]\,\text{S/m}$	$[0.06, 0.16]\,\text{S/m}$	$[0.4, 0.6]\,\text{S/m}$

We remark that the 3-ellipse samples are designed as prior information of general structures in the thorax. Specifically, the ellipses e1 and e2 are used to mimic two lung lobes, and the ellipse e3 is used to mimic the heart. We generated a total number of 4096 training samples, consisting of 3072 (75%) 1-circle samples and 1024 (25%) 3-ellipse samples.

Before training, EIT forward solver was run to generate synthetic data corresponding to the training samples. No noise was added to the data. The maximum iteration number of SDL-EIT training was set as 10. The initial guess was set uniformly as 0.2 S/m for all the training samples. The damping factor α in (16) was set as one-sixth of the maximum singular value of $\Delta \mathbf{D}_k$. Positive constraint was imposed to the conductivity in the training process. The iteration was forced to terminate if the data loss (12) decreased below 0.001, or the maximum iteration number was reached.

The algorithm was implemented using Matlab R2016a (MathWorks, Inc.) on a desktop personal computer equipped with Intel(R) Core(TM) i5-6500 CPU and Windows 7 operating system. The Matlab Parallel Computing Toolbox was used to parallelize the forward simulation in each iteration. The whole training process took 32 minutes after 10 iterations. The training losses are shown in Fig. 2.

B. Test

Firstly, the descent directions were tested using data from several models unseen in the training, as shown in the first row of Fig. 3. Synthetic data with 1% white Gaussian noise [33] were used in the test. The test results are shown in the second row of Fig. 3. Overall, the algorithm can produce reasonable
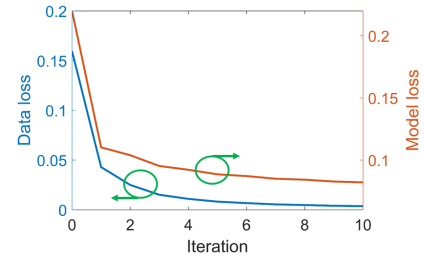

Fig. 2. Training losses of the 2D simulation experiment.

results on these models. This suggests that the learned descent directions can generalize to data unseen in the training.
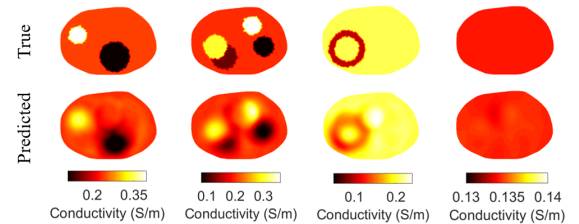

Fig. 3. Test results of some models unseen in the training.

Secondly, synthetic data from 2D thorax models were used to test the learned descent directions. The traditional Gauss–Newton inversion (GNI) method was also performed for comparison purpose. Specifically, an objective function was constructed with the total variation (TV) regularization [32]:

$$C(\sigma) = ||\mathbf{s}(\sigma) - \mathbf{d}_*||^2 + \lambda \text{TV}_\beta(\sigma), \qquad (17)$$

where $\text{TV}_\beta(\sigma) = \int_\Omega \sqrt{|\nabla\sigma|^2 + \beta} \ (\beta > 0)$ is the approximated TV function, and λ is the regularization parameter. The regularization parameter is determined heuristically by inspecting the data loss and reconstructed images. The maximum iteration number for GNI is set as 20. A line search technique is used to guarantee the decrease of the objective function. For more details on the application of GNI for EIT, please refer to [33]–[36].

Both for SDL-EIT and GNI, the iteration will stop if the data loss is below the noise threshold. The initial guess for both the two methods is set as 0.2 S/m.

The simulated 2D thorax models are shown in the first column of Fig. 4. All the models have an orientation in accordance with the DICOM format. In the dorsal part of the left lung, the "pleural effusion" model contains a high-conductivity region due to the accumulation of liquid in the pleural cavity. In the right lung of the "pneumothorax" model, the conductivity is abnormally low due to the accumulation of air. The "pulmonary edema" model shows an abnormally high and nonuniform conductivity distribution in the whole lung region.

The reconstruction results of the 2D thorax models under 1%, 3%, and 5% white Gaussian noise are shown in Fig. 4. The reconstructed images are evaluated using the relative image error (RIE):

$$\text{RIE} = \frac{1}{N_p} \sum_{i=1}^{N_p} \frac{|\sigma_{r(i)} - \sigma_{*(i)}|}{|\sigma_{*(i)}|}, \qquad (18)$$

where $\sigma_{r(i)}$ and $\sigma_{*(i)}$ are the ith pixel values of the reconstructed and true conductivity images, respectively, and N_p is the total number of pixels. The calculated RIE values are shown below the images. It can be seen that both SDL-EIT and TV-regularized Gauss–Newton inversion (TV-GNI) can well reconstruct the lung regions under different conditions when the noise level is relatively low (e.g., 1%). When the noise level increases to 3% or 5%, we can see obvious boundary artifacts and distortion of lung regions in the reconstructed images of TV-GNI. As a comparison, the reconstructed images of SDL-EIT are less sensitive to noise.

The image reconstruction process can be accelerated using SDL-EIT. In the 2D examples shown above, the time for each iteration of SDL-EIT online inversion is 0.18 s, whereas the time for each iteration of TV-GNI is 2.67 s. In each iteration of SDL-EIT online inversion (see (13)), one forward problem needs to be solved in order to calculate the data residual, and then a matrix-vector multiplication needs to be performed to calculate the search direction. There is no need to calculate the Jacobian matrix and solve the matrix equation for search direction as in the Gauss–Newton inversion method.

C. Proportioning of Samples

The ratio of the two types of samples (cf. Fig. 1) has a significant effect on the performance of the learned descent directions. To explain this, we conducted one experiment, in
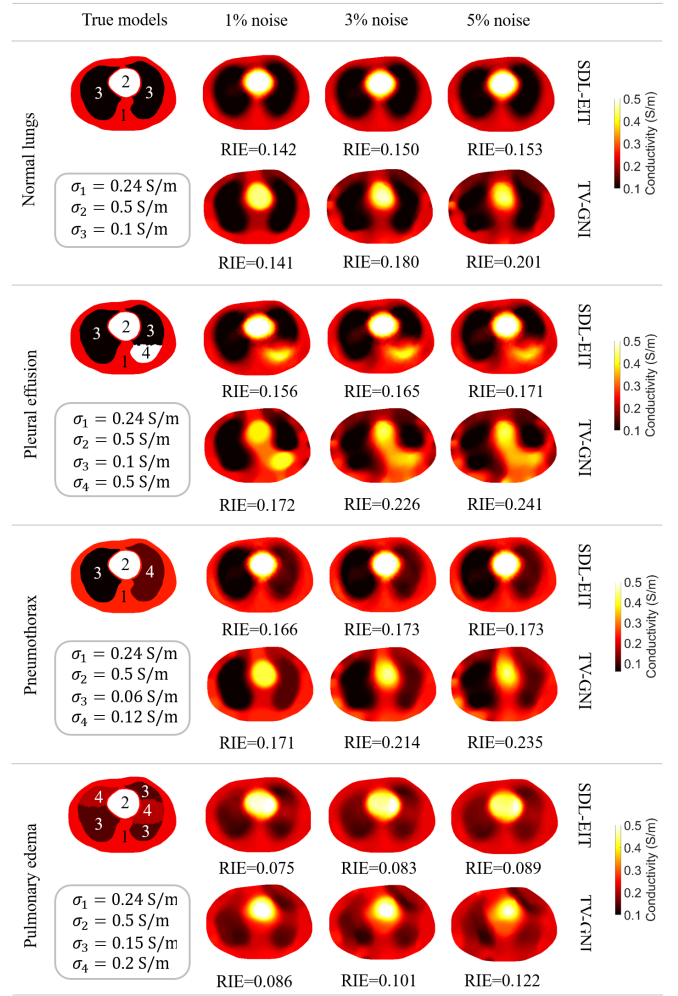

Fig. 4. Comparison of inversion results between supervised descent learning EIT (SDL-EIT) and TV-regularized Gauss–Newton inversion (TV-GNI) using simulated 2D thorax models. The synthetic data contain 1%, 3%, and 5% white Gaussian noise, respectively. The relative image error (RIE) is calculated for each reconstructed image.

which the size of training data set is fixed, while the proportion of 1-circle samples is increased gradually. Specifically, a coefficient is defined as $\eta = N_{circ}/N_{total}$, where N_{circ} is the number of 1-circle samples, and N_{total} is the total number of samples. In the experiment, we fixed $N_{total} = 4096$. The parameters of the samples are the same as those described in Section IV-A. Then training was performed using data sets with different proportioning of samples, and the training settings were kept the same.

Several models were used to test the learned descent directions from the above experiment, and some of the results are shown in Fig. 5. It can be seen that when the proportion of 1-circle samples is relatively low (e.g., $\eta = 0, 0.25$), the learned descent directions show relatively poor generalization ability. With the increase of the proportion of 1-circle samples (e.g., $\eta = 0.5, 0.75$), the accuracy of the results improves significantly. However, the results deteriorate when there are only 1-circle samples in the training data set ($\eta = 1$). The above observations indicate that 1-circle samples can improve

the generalization ability of the learned descent directions, whereas 3-ellipse samples are important to the accuracy of results. In fact, the 3-ellipse samples serve as the prior information of human thoracic structures. In practice, a relatively small portion (e.g., 25%∼50%) of 3-ellipse samples will significantly enhance the accuracy of inversion results.
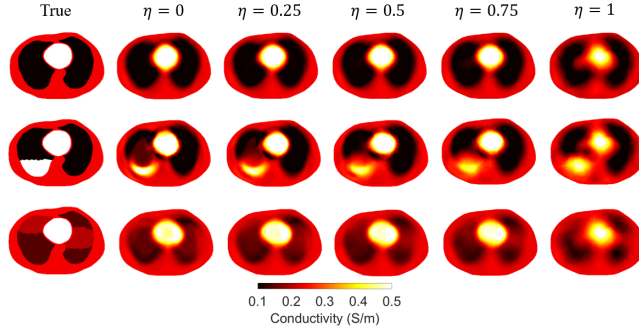

Fig. 5. Inversion results of SDL-EIT using training data sets with different proportioning of samples. The parameter η is the proportion of 1-circle samples in the whole data set. The data used for inversion are corrupted with 1% noise.

D. Study on Initial Guess

Uniform initial guess contains no structural information of the thorax, and different uniform initial guesses have little influence on the solution. Since the thorax has two lung lobes and one heart, we may use a weak structural initial guess which models the lungs and heart as ellipses. Besides, strong structural initial guess can be constructed if we have other sources of image of the patient, such as the CT scan image. Let us take the "pleural effusion" model shown in Fig. 4 for example. In the first column of Fig. 6, we show a weak structural initial guess and a strong structural initial guess, respectively. The initial guesses are used for both training and test. The training data and training settings are the same as those used in Section IV-A. Fig. 6 also shows the inversion results of structural initializations. It can be seen that the inversion result of weak structural initialization is almost the same as that of uniform initialization (see Fig. 4). However, the inversion result of strong structural initialization is significantly more accurate. This suggests the possibility of integrating structural information through the initial guess on the condition that the information is accurate enough.

We also compared the learned $\mathbf{K}_k$ matrices (see (9)) for different initializations. Basically, the patterns of $\mathbf{K}_k$ have notable difference in each of the first several iterations. As the iteration proceeds, the patterns become more and more similar. This can be explained using (9). From (9), we can see that the regression result in each iteration depends on the conductivity models in the current iteration. For different initial guesses, the conductivity models have large difference in the first several iterations, and so do the regressed $\mathbf{K}_k$ matrices. As the iteration progresses, the conductivity models become closer and closer to the correct models. As a result, the regressed $\mathbf{K}_k$ matrices will become more and more similar.
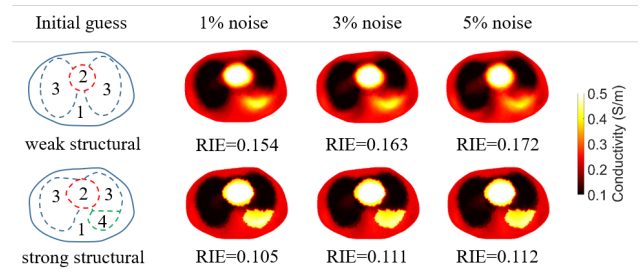

Fig. 6. Inversion results of the "pleural effusion" model (cf. Fig. 4) using structural initializations. Conductivity settings of the initial guesses: "weak structural": σ_1=0.2 S/m, σ_2=0.8 S/m, σ_3=0.05 S/m; "strong structural": σ_1=0.2 S/m, σ_2=0.8 S/m, σ_3=0.05 S/m, σ_4=0.8 S/m.

E. Choice of Parameter α

In Section III-C, a damping factor α is introduced to stabilize the solution of linear regression in the training phase. Here we study the sensitivity of solution to the choice of this parameter. The training data and training settings are the same as those used in Section IV-A, except for the α value. The value of α is set adaptively as a number times the maximum singular value of $\Delta\mathbf{D}_k$. The numerical models shown in Fig. 4 are used to test the learned descent directions. Fig. 7 plots the inversion error with different choices of α value. Here the data used for inversion are corrupted with 3% noise. When other levels of noise are added, similar results can be obtained. It can be seen from Fig. 7 that the proper range of α value is 0.1∼3 times the maximum singular value of $\Delta\mathbf{D}_k$.
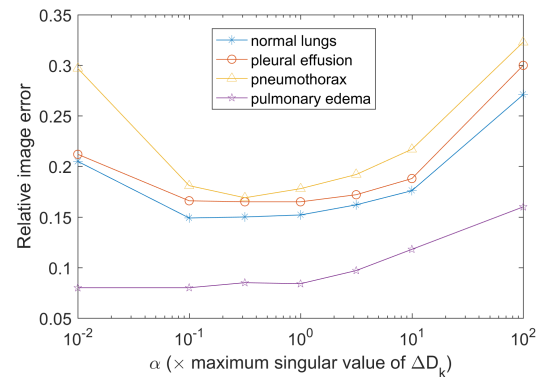

Fig. 7. Inversion error when different α values are used in the training. The data used for inversion are corrupted with 3% noise.

F. Ill-Posedness in Training Data

Due to the ill-posedness of EIT inverse problem, different conductivity models may correspond to the same (or similar) data in the training data set. In this case, the learned descent directions may find an average between these models that will not be a solution at all. To study if such samples exist in the training data set (used in Section IV-A), we compute the data difference $||\mathbf{d}_*^i - \mathbf{d}_*^j||/||\mathbf{d}_*^j||$ and model difference $||\boldsymbol{\sigma}_*^i - \boldsymbol{\sigma}_*^j||/||\boldsymbol{\sigma}_*^j||$ of any two samples i and j, and then generate the scatter plots (data difference as x-data and model

difference as y-data), as shown in Fig. 8. In Case 1, the scattered points converge to the coordinate origin, meaning the model difference decreases with the decrease of data difference generally. Besides, we cannot observe sample pairs whose data difference is zero and meanwhile the model difference is nonzero. In Case 2–4, there are no scattered points around the coordinate origin, meaning both the data difference and model difference are relatively large. It is worth noting that there exist sample pairs in Case 1 whose data difference is small whereas the model difference is relatively large (e.g., samples marked by the red box), which may cause inaccuracy to the learned descent directions. However, test results show that SDL-EIT can successfully invert the conductivity distributions of these samples. This indicates that SDL-EIT is able to differentiate small differences in the data.
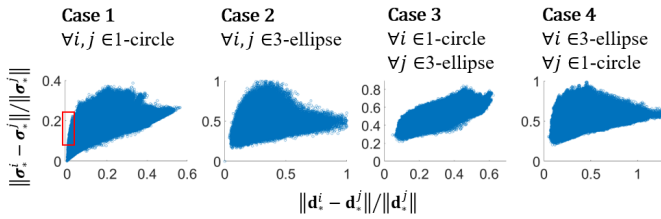

Fig. 8. Scatter plot of data difference (the horizontal axis) and model difference (the vertical axis) of training samples used in Section IV-A.

In the design of training data set, we should minimize the number of samples whose conductivity models are different whereas the corresponding data are the same. The above analysis method provides us a potential way to optimize the training data set.

V. 3D SIMULATION EXPERIMENT

A. Training

The training samples are defined on a 3D thoracic shaped finite-element model, as shown in Fig. 9(a). The interior mesh is arbitrarily arranged and contains no anatomical structures. Sixteen rectangular electrodes are attached around the boundary of the model. The design of the 3D training data set is extended from the 2D case, as illustrated in Fig. 9(b). Briefly, the training data set contains two types of samples: 1-sphere samples and 3-ellipsoid samples. The 1-sphere sample contains only one sphere with random location. The radius of the sphere is fixed as 0.04 m. Based on our experience, this radius can be set as other proper values. The conductivities of the sphere and the background are uniform randomly sampled from [0.06,0.36] S/m and [0.2,0.25] S/m, respectively. The 3-ellipsoid sample contains three ellipsoids with random locations, sizes, rotation angles, and conductivities. Ranges of these parameters are listed in Table II. In the 3-ellipsoid samples, the background conductivity is uniform randomly sampled from [0.2,0.25] S/m. We generated a total number of 16384 training samples, consisting of 12288 (75%) 1-sphere samples and 4096 (25%) 3-ellipsoid samples.

The training setups are as follows. The maximum iteration number was set as 10. The initial guess was set uniformly as 0.2 S/m. The damping factor α in (16) was set as one-sixth of
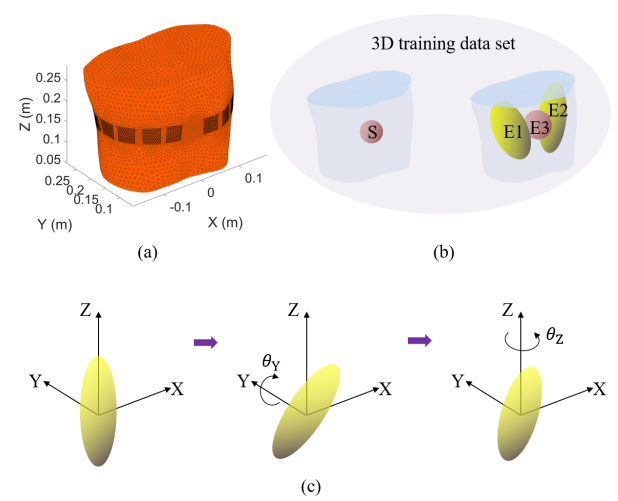

Fig. 9. Illustration of the 3D training data set. (a) Finite-element model on which training samples are defined. The mesh contains 15430 nodes and 72563 tetrahedral elements. Sixteen rectangular electrodes are around the boundary of the model. (b) The whole data set contains two types of samples: 1-sphere samples and 3-ellipsoid samples. The 1-sphere samples contain one sphere with random location and conductivity. The 3-ellipsoid samples contain three ellipsoids with random locations, sizes, rotation angles, and conductivities. (c) Rotation scheme for the ellipsoids. The ellipsoids are first rotated around the Y-axis by θ_Y and then rotated around the Z-axis by θ_Z.

the maximum singular value of $\Delta \mathbf{D}_k$. The training took 56.9 hours after 10 iterations. The final data loss and model loss are 0.09% and 4%, respectively.

B. Test

The learned descent directions were tested using 3D thorax models with the heart and two lung lobes. The boundary shape and electrode positions of the 3D thorax models are the same as those of the model used for training sample generation. In Fig. 10, several lung conditions are modeled and used to test the learned descent directions. The image reconstruction results of these lung conditions are shown in Fig. 11. Relative image error (see (18)) is also calculated for each reconstructed image. Although 3D image reconstructions were performed, we only visualized the reconstructed images on a 2D plane around the electrodes as the reconstruction accuracy quickly decreased away from the electrodes.
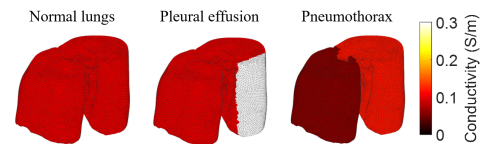

Fig. 10. Three-dimensional lung models with different conditions. The upper parts of the lungs are truncated.

It can be seen from the SDL-EIT inversion results that different conditions of the lung can be well reflected, and both the shape and conductivity of the interior structures are well reconstructed. In comparison, the results of TV-regularized Gauss–Newton inversion (TV-GNI) show a relatively low

| Ellipsoid / Parameter	E1	E2	E3
Center location	$\{(x, y, z)\|x \in [-0.089, -0.062]\,\mathrm{m}, y \in [0.15, 0.184]\,\mathrm{m}, z \in [0.175, 0.208]\,\mathrm{m}\}$	$\{(x, y, z)\|x \in [0.043, 0.068]\,\mathrm{m}, y \in [0.141, 0.176]\,\mathrm{m}, z \in [0.156, 0.196]\,\mathrm{m}\}$	$\{(x, y, z)\|x \in [-0.011, 0.01]\,\mathrm{m}, y \in [0.124, 0.144]\,\mathrm{m}, z \in [0.171, 0.195]\,\mathrm{m}\}$
Size	x-radius $\in [0.04, 0.07]$ m, y-radius $\in [0.06, 0.12]$ m, z-radius $\in [0.05, 0.09]$ m	x-radius $\in [0.04, 0.07]$ m, y-radius $\in [0.06, 0.12]$ m, z-radius $\in [0.05, 0.09]$ m	x-radius $\in [0.02, 0.06]$ m, y-radius $\in [0.02, 0.06]$ m, z-radius $\in [0.02, 0.06]$ m
Rotation angle	y-rotation $\in [-\pi/6, \pi/6]$ rad, z-rotation $\in [0, 2\pi)$ rad	y-rotation $\in [-\pi/6, \pi/6]$ rad, z-rotation $\in [0, 2\pi)$ rad	y-rotation $\in [-\pi/6, \pi/6]$ rad, z-rotation $\in [0, 2\pi)$ rad
Conductivity	[0.06, 0.16] S/m	[0.06, 0.16] S/m	[0.4, 0.6] S/m
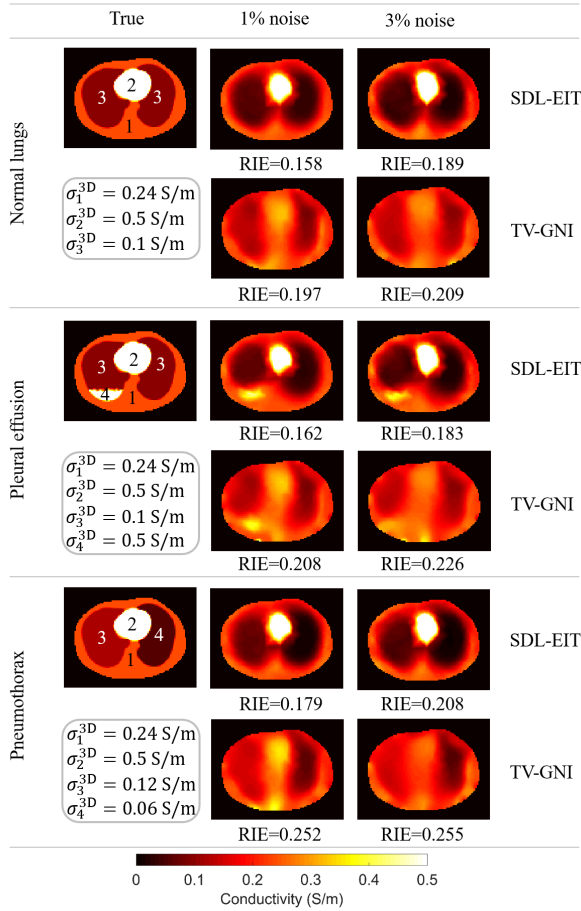
Fig. 11. Three-dimensional reconstruction results using SDL-EIT and TV-regularized Gauss–Newton inversion (TV-GNI) with 1% and 3% white Gaussian noise in the synthetic data. The reconstructed images are visualized on a 2D plane around the electrodes. The relative image error (RIE) is calculated for each reconstructed image.

contrast although different pathologies can also be recognized. This is because the 3D inversion is much more ill-posed than in the 2D case. As a result, the solutions of TV-GNI are easily affected by noise in data. This can be clearly seen from the low reconstruction accuracy of the heart because boundary measurements are insensitive to the heart. For SDL-EIT, structural prior of the thorax can be learned through training data. Besides, the training process of SDL-EIT allows the learning of global descent directions to some extent, which further enhances its accuracy and anti-noise performance.

The time cost for each iteration of SDL-EIT online inversion is 5.7 s, whereas the time cost for each iteration of TV-GNI is 310.3 s. In our experiments, both SDL-EIT and TV-GNI converged within 10 iterations.

VI. IN VIVO EXPERIMENT

The measured data of a normal male subject were used to test the algorithm. The data were acquired from a joint EIT-CT experiment in Tsinghua University Hospital. In the experiment, EIT data were first collected from the subject with sitting and supine postures, respectively. The EIT measurement system is homemade and used for research. The system is designed for 16 electrodes. It operates at 20 kHz and utilizes the adjacent injection-measurement protocol. The root mean square (RMS) value of the injected currents is 2 mA. After the EIT measurement, CT scan was performed when the subject was holding breath after inhalation, with the supine posture unchanged. The above experiment was approved by the Institution Review Board of Tsinghua University. Informed consent was obtained from the subject.

The CT scan images are used to determine the boundary shape of the thorax as well as the electrode positions. No further anatomical information was exploited from the CT scan images. The design of training data set is similar to that in the 3D simulation experiment (see Section V-A). The total number of training samples is 16384, including 12288 (75%) 1-sphere samples and 4096 (25%) 3-ellipsoid samples. The training setups are the same as in the 3D simulation experiment.

Both SDL-EIT and TV-GNI were performed using the EIT measured data under sitting and supine postures. Fig. 12 shows the inversion results when the measured data are selected at the end of inspiration. The CT scan image is also shown as a reference for the reconstructed EIT images.

It can be seen from Fig. 12 that the reconstructed images of SDL-EIT correlate well with the CT scan image. Besides, the conductivity distributions vary with posture. This can be attributed to the redistribution of air and liquid in the thorax due to gravity. As a comparison, the reconstructed images of TV-GNI suffer from low accuracy, and the lung region cannot be properly reconstructed.

In order to study the variation of lung conductivity with respiration, SDL-EIT was performed using data from one

This article has been accepted for publication in a future issue of this journal, but has not been fully edited. Content may change prior to final publication. Citation information: DOI 10.1109/TBME.2020.3027827, IEEE Transactions on Biomedical Engineering

SUPERVISED DESCENT LEARNING EIT   9
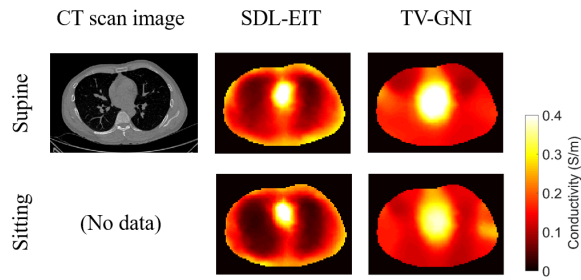
Fig. 12. Reconstruction results using real measurements of a human thorax with different postures. (SDL-EIT: supervised descent learning EIT; TV-GNI: TV-regularized Gauss–Newton inversion)
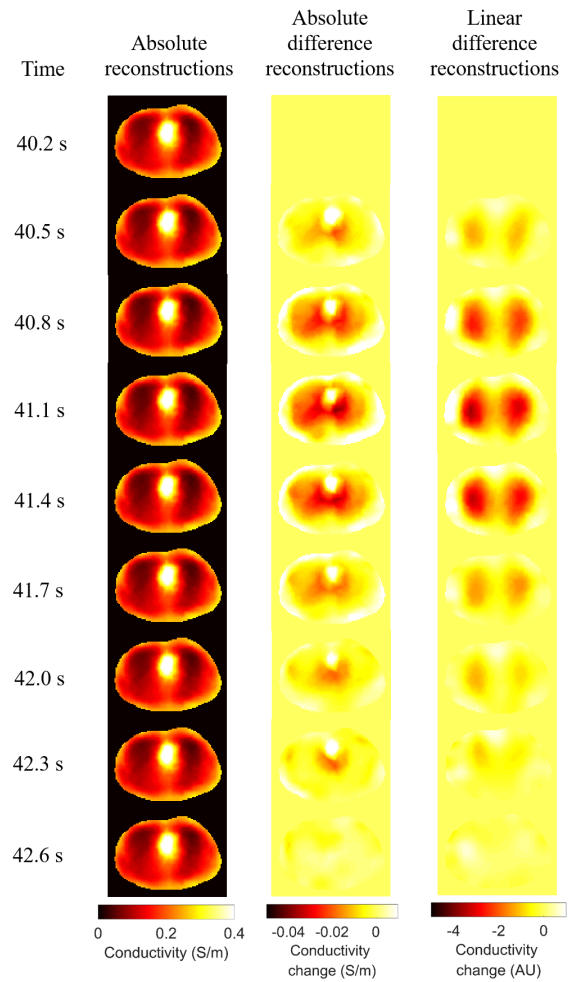

Fig. 13. SDL-EIT image reconstruction in one respiratory cycle (40.2 s: end of expiration; 41.1 s: end of inspiration; 42.6 s: end of expiration). To obtain the absolute difference images, the absolute image at 40.2 s is used as the reference and subtracted from other absolute images. The linear difference images are obtained using one-step Gauss–Newton inversion method with Tikhonov regularization. (AU: arbitrary unit)

respiratory cycle (supine posture), and absolute images were reconstructed at several different time points. Then the absolute image at the start of inspiration is selected as the reference, which is subtracted from other absolute images, leading to the absolute difference images. These images are shown in the second column of Fig. 13. For comparison, linear difference images were obtained using one-step Gauss–Newton inversion method with Tikhonov regularization. It can be seen from the absolute difference images that the reconstructed absolute lung conductivities vary with respiration, and the variation agrees well with the linear difference images. This indicates that SDL-EIT is capable of distinguishing small variations in the data caused by respiration. Comparing with linear difference images, the absolute difference images show quantitative conductivity changes and a seemingly higher spatial resolution.

VII. Discussion

In SDL-EIT, prior information can be integrated flexibly through the training data. It is an important issue that how to design an effective training data set. First, we need to exploit some prior information for a certain problem. The thorax imaging problem has an advantage that the human thorax has remarkable features, i.e., the thorax usually contains two lung lobes and one heart, and their positions in the thorax are relatively fixed. Second, the strength of prior information should be proper. In this work, the 3-ellipse (3-ellipsoid) samples provide prior information about general thoracic structures, whereas the 1-circle (1-sphere) samples provide no such information. The proportion of the two types of samples controls the strength of prior information. This has been illustrated in Fig. 5. If the proportion of the 3-ellipse (3-ellipsoid) samples is too small, the prior information of thoracic structures is too weak to shape the descent directions ($\mathbf{K}_k$ matrices) and thus the inversion process sufficiently. However, a too large proportion of those samples will decrease the generalization ability of the descent directions. Based on our experience, SDL-EIT works well when the proportion of the 3-ellipse (3-ellipsoid) samples is 25%~50%.

In this work, uniform initial guess is used in the training and test. When we have little prior information of the interior structure of the thorax, uniform initial guess is a convenient choice. However, structural initial guess may be constructed if other sources of information (e.g., CT scan images) are

available. This provides us another chance to integrate prior information into the algorithm.

The EIT inverse problem is ill-posed. As a result, conductivity models with distinct difference may correspond to the same data. If the training data set contains such samples, the learned descent directions tend to find an average between them which is probably not a meaningful solution. In the design of training data set, the number of such samples should be minimized. In the training data set used in this work, there are no samples whose conductivity distributions are different whereas the corresponding data are the same. The analysis method used provides us a potential way to optimize the training data set.

There are still limitations of current work. Firstly, modeling factors such as the boundary shape and electrode positions are treated as prior information in this work. In fact, SDL-EIT is sensitive to errors in these factors, similar to the behavior of Gauss–Newton inversion method. In the future,

two possible technical paths may be taken to improve the practical usability of the algorithm: (1) instead of using CT scan images, determine the boundary shape and electrode positions using more convenient and fast methods, such as the 3D scan technique; (2) incorporate mechanisms into the algorithm to handle modeling errors.

Secondly, we only evaluate SDL-EIT using measured data from one normal subject in this work. Although promising results are obtained, it is expected to evaluate the algorithm using more measured data, including those from patients.

VIII. Conclusion

SDL-EIT has the advantage of integrating prior information into the inversion flexibly through the training data. The training data set designed in this work reflects the prior information of human thorax and is suitable for thoracic imaging. Besides, the inversion process of SDL-EIT is fast once the machine learning model has been trained. Comparing with the Gauss–Newton inversion (GNI) method, SDL-EIT avoids the computation of Jacobian and Hessian matrices, which is time-consuming. By inverting synthetic data, SDL-EIT shows better reconstruction accuracy and anti-noise performance than the GNI method. By inverting measured data, SDL-EIT shows promising results for human thoracic imaging.

Acknowledgment

References

[1] J. A. Victorino et al, "Imbalances in regional lung ventilation: a validation study on electrical impedance tomography," *Am. J. Respir. Crit. Care Med.*, vol. 169, no. 7, pp. 791–800, 2004.

[2] I. Frerichs et al, "Regional lung perfusion as determined by electrical impedance tomography in comparison with electron beam CT imaging," *IEEE Trans. Med. Imag.*, vol. 21, no. 6, pp. 646–652, 2002.

[3] Y. Zou and Z. Guo, "A review of electrical impedance techniques for breast cancer detection," *Med. Eng. Phys.*, vol. 25, no. 2, pp. 79–90, 2003.

[4] A. P. Bagshaw et al, "Electrical impedance tomography of human brain function using reconstruction algorithms based on the finite element method," *NeuroImage*, vol. 20, no. 2, pp. 752–764, 2003.

[5] R. V. Davalos et al, "Electrical impedance tomography for imaging tissue electroporation," *IEEE Trans. Biomed. Eng.*, vol. 51, no. 5, pp. 761–767, 2004.

[6] S. Siltanen et al, "An implementation of the reconstruction algorithm of A Nachman for the 2D inverse conductivity problem," *Inverse probl.*, vol. 16, no. 3, p. 681, 2000.

[7] J. L. Mueller et al, "A direct reconstruction algorithm for electrical impedance tomography," *IEEE Trans. Med. Imag.*, vol. 21, no. 6, pp. 555–559, 2002.

[8] M. Alsaker and J. L. Mueller, "A D-bar algorithm with a priori information for 2-dimensional electrical impedance tomography," *SIAM J. Imaging Sci.*, vol. 9, no. 4, pp. 1619–1654, 2016.

[9] S. J. Hamilton et al, "Incorporating a spatial prior into nonlinear D-bar EIT imaging for complex admittivities," *IEEE Trans. Med. Imag.*, vol. 36, no. 2, pp. 457–466, 2017.

[10] M. Hanke and M. Brühl, "Recent progress in electrical impedance tomography," *Inverse probl.*, vol. 19, no. 6, p. S65, 2003.

[11] B. Gebauer and N. Hyvönen, "Factorization method and irregular inclusions in electrical impedance tomography," *Inverse probl.*, vol. 23, no. 5, pp. 2159–2170, 2007.

[12] B. Harrach, "Recent progress on the factorization method for electrical impedance tomography," *Comput. Math. Method. M.*, vol. 2013, 2013.

[13] A. Abbasi et al, "An inverse solution for 2D electrical impedance tomography based on electrical properties of material blocks," *J. Appl. Sci.*, vol. 9, no. 10, pp. 1962–1967, 2009.

[14] S. Martin and C. T. Choi, "A novel post-processing scheme for two-dimensional electrical impedance tomography based on artificial neural networks," *PloS One*, vol. 12, no. 12, p. e0188993, 2017.

[15] S. Martin and C. T. Choi, "A post-processing method for three-dimensional electrical impedance tomography," *Sci. Rep.*, vol. 7, no. 1, p. 7212, 2017.

[16] S. J. Hamilton and A. Hauptmann, "Deep D-Bar: Real-time electrical impedance tomography imaging with deep neural networks," *IEEE Trans. Med. Imag.*, vol. 37, no. 10, pp. 2367–2377, 2018.

[17] Z. Wei et al, "Dominant-current deep learning scheme for electrical impedance tomography," *IEEE Trans. Biomed. Eng.*, vol. 66, no. 9, pp. 2546–2555, 2019.

[18] C. Tan et al, "Image reconstruction based on convolutional neural network for electrical resistance tomography," *IEEE Sens. J.*, vol. 19, no. 1, pp. 196–204, 2018.

[19] X. Li et al, "An image reconstruction framework based on deep neural network for electrical impedance tomography," in *ICIP 2017*, Beijing, China, 2017, pp. 3585–3589.

[20] J. K. Seo et al, "A learning-based method for solving ill-posed nonlinear inverse problems: a simulation study of lung eit," *SIAM J. Imaging Sci.*, vol. 12, no. 3, pp. 1275–1295, 2019.

[21] G. Klosowski and T. Rymarczyk, "Using neural networks and deep learning algorithms in electrical impedance tomography," *Informatyka, Automatyka, Pomiary w Gospodarce i Ochronie Srodowiska*, vol. 7, pp. 99–102, 2017.

[22] T. Rymarczyk et al, "Comparison of selected machine learning algorithms for industrial electrical tomography," *Sensors*, vol. 19, no. 7, p. 1521, 2019.

[23] L. Bar and N. Sochen, "Unsupervised deep learning algorithm for PDE-based forward and inverse problems," *arXiv preprint arXiv:1904.05417*, 2019.

[24] T. A. Khan and S. H. Ling, "Review on electrical impedance tomography: artificial intelligence methods and its applications," *Algorithms*, vol. 12, no. 5, p. 88, 2019.

[25] X. Xiong and F. De la Torre, "Supervised descent method and its applications to face alignment," in *Proc. CVPR*, Portland, OR, USA, 2013, pp. 532–539.

[26] R. Guo et al, "Supervised descent learning technique for 2-D microwave imaging," *IEEE Trans. Antennas Propag.*, vol. 67, no. 5, pp. 3550–3554, 2019.

[27] R. Guo et al, "Application of supervised descent method to transient electromagnetic data inversion," *Geophysics*, vol. 84, no. 4, pp. E225–E237, 2019.

[28] K.-S. Cheng et al, "Electrode models for electric current computed tomography," *IEEE Trans. Biomed. Eng.*, vol. 36, no. 9, pp. 918–924, 1989.

[29] P. J. Vauhkonen et al, "Three-dimensional electrical impedance tomography based on the complete electrode model," *IEEE Trans. Biomed. Eng.*, vol. 46, no. 9, pp. 1150–1160, 1999.

[30] M. Soleimani et al, "Improving the forward solver for the complete electrode model in EIT using algebraic multigrid," *IEEE Trans. Med. Imag.*, vol. 24, no. 5, pp. 577–583, 2005.

[31] A. Adler et al, "GREIT: a unified approach to 2D linear EIT reconstruction of lung images," *Physiol. Meas.*, vol. 30, no. 6, p. S35, 2009.

[32] L. I. Rudin et al, "Nonlinear total variation based noise removal algorithms," *Physica D*, vol. 60, no. 1–4, pp. 259–268, 1992.

[33] A. Borsic et al, "In vivo impedance imaging with total variation regularization," *IEEE Trans. Med. Imag.*, vol. 29, no. 1, pp. 44–53, 2010.

[34] D. Liu et al, "Nonlinear difference imaging approach to three-dimensional electrical impedance tomography in the presence of geometric modeling errors," *IEEE Trans. Biomed. Eng.*, vol. 63, no. 9, pp. 1956–1965, 2016.

[35] D. Liu et al, "A parametric level set method for electrical impedance tomography," *IEEE Trans. Med. Imag.*, vol. 37, no. 2, pp. 451–460, 2017.

[36] K. Zhang et al, "Three-dimensional electrical impedance tomography with multiplicative regularization," *IEEE Trans. Biomed. Eng.*, vol. 66, no. 9, pp. 2470–2480, 2019.